Remote Sensing of Induced Liquefaction: TLS and SfM for a Full-Scale Blast Test

Published Version:
Pesci A., Teza G., Loddo F., Rollins K.M., Andersen P., Minarelli L., et al. (2022). Remote Sensing of Induced Liquefaction: TLS and SfM for a Full-Scale Blast Test. JOURNAL OF SURVEYING ENGINEERING-ASCE, 148(1), 1-13 [10.1061/(ASCE)SU.1943-5428.0000379].

Availability:
This version is available at: https://hdl.handle.net/11585/861291 since: 2022-02-19

Published:
DOI: http://doi.org/10.1061/(ASCE)SU.1943-5428.0000379

Remote sensing of induced liquefaction: TLS and SfM for a full scale blast test

Arianna Pesci[1], Giordano Teza[2], Fabiana Loddo[3], Kyle Rollins[4], Paul Andersen[5], Luca Minarelli[6], Sara Amoroso[7]

[1] Researcher, Istituto Nazionale di Geofisica e Vulcanologia, Sezione di Bologna, Via Donato Creti, 12, 40128 Bologna, Italy (Corresponding author). http://orcid.org/0000-0003-1863-3132. Email: arianna.pesci@ingv.it

[2] Researcher, Department of Physics and Astronomy, University of Bologna, Viale Berti Pichat 6/2, 40127 Bologna, Italy. http://orcid.org/0000-0002-6902-5033. Email: giordano.teza@gmail.com

[3] Technologist, Istituto Nazionale di Geofisica e Vulcanologia, Sezione di Bologna, Via Donato Creti, 12, 40128 Bologna, Italy. http://orcid.org/0000-0002-1153-1021. Email: fabiana.loddo@ingv.it

[4] Professor, Department of Civil and Environmental Engineering, Brigham Young University, 430 Engineering Building, Provo, UT 84602, USA. http://orcid.org/0000-0002-8977-6619. Email: rollinsk@byu.edu

[5] Research Assistant, Department of Civil and Environmental Engineering, Brigham Young University, 430 Engineering Building, Provo, UT 84602, USA. http://orcid.org/0000-0002-9084-4084. Email: paul.andersen@byu.edu

[6] Temporary Research Assistant, Istituto Nazionale di Geofisica e Vulcanologia, Sezione Roma1, Sede L'Aquila, Viale Francesco Crispi 43, 67100 L'Aquila Italy. ORCID: 0000-0003-3602-9975. Email: luca.minarelli@ingv.it

[7] Assistant Professor, Department of Engineering and Geology, University of Chieti-Pescara, Viale Pindaro 42, 65129 Pescara, Italy; Research Associate, Istituto Nazionale di Geofisica e Vulcanologia, Sezione Roma 1, Sede L'Aquila, Viale Francesco Crispi 43, 67100 L'Aquila, Italy. ORCID: 0000-0001-5835-079X. Email: sara.amoroso@unich.it

Abstract

Terrestrial Laser Scanning (TLS) and drone-based Structure from Motion photogrammetry (SfM) allowed the study of soil deformations due to blast-induced liquefaction during an experiment carried out on 4 June 2018. The research aimed at both evaluating the measurement quality and estimating the Rammed Aggregate Piers (RAPs) effectiveness in mitigating the effects of soil liquefaction. These effects mainly consist in subsidence and deposits of ejected and extruded materials. The comparison between multi-temporal 3D models provided surface variation maps and volume changes. In addition, classical topographical levelling allowed the measurement of sub-surface vertical displacement along a specific cross-section. The results pointed out a significant reduction, higher than 50%, of soil deformation in areas improved by RAPs installation; moreover, the corresponding volume variations were no more than about 37% of those occurred in the not

improved area. Finally, a critical comparison between remote sensing and levelling suggested that surface variation maps could underestimate the area lowering up to 15% in this kind of terrains.

Author keywords: Blast Test; Terrestrial Laser Scanning; Structure-from-Motion (SfM); Ground deformation; Soil Liquefaction; Soil compaction.

Introduction

Soil liquefaction occurs in cases where a saturated soil temporarily loses strength and stiffness caused by a sudden increase in excess porewater pressure due to, e.g., an earthquake or an underground explosion. Liquefaction in saturated sandy deposits can induce severe damage to structures during earthquakes. For this reason, Eurocode 8 (EN 2004), related to design of structures for earthquake resistance, requires the quantitative evaluation of post-liquefaction settlements. The studies on soil liquefaction are therefore important from both a scientific and an engineering application point of view. However, these studies are difficult to implement for several reasons, among which there are the stochastic nature of the earthquake loading, the uncertainties related to geotechnical methods used to characterize the soil, the fact that often no data are available to allow comparison between the pre-seismic and post-seismic conditions, and the need for reliable numerical models (Győri et al. 2011). Blast tests, in which controlled blasting is carried out by suitably positioned underground charges, are relatively recent, but they have already proved to be of great importance (see e.g. Ashford et al. 2004; Saftner et al. 2015; Wentz et al. 2015; Amoroso et al. 2017; 2020a).

Despite the potentially disastrous loss of soil strength and stiffness which can occur at the time of the phenomenon that induces liquefaction, controlled blasting can also be beneficial as a ground improvement technique for densification in clean sands (Finno et al. 2016). As porewater pressures dissipate upwards following blasting, the sand reconsolidates to a denser more compact state. The ground surface deformation plays an important role in compaction effect evaluation as well as the estimate the subsoil changes that could be indirectly inferred (Pesci et al. 2018). In general, mapping aimed at evaluating local subsidence is an important task to ensure building in suitable areas. Examples are the recognition of sinkholes (Gutierrez et al. 2018) and analysis of liquefaction susceptibility (Giona Bucci et al. 2018). Advanced statistical methods of data analysis are also used for this purpose (Hu and Lui 2019). Dealing with remote sensing suitable technics for monitoring surface variations, Terrestrial Laser Scanning (TLS), Structure-from-Motion photogrammetry (SfM) and Ground-Based Interferometric Synthetic Aperture Radar (InSAR) are highly efficient.

TLS provides point clouds, i.e. sets of XYZ coordinates of numerous points sampled on the observed surface (Vosselman and Maas 2010). Currently available instruments can measure 10^4-10^6 points per second with 0.1-1 cm precision. Topographic mapping and spatial analyses can be carried out directly on the point cloud or also on a digital model generated from the point cloud, in particular a 2.5D model, which is the case of a Digital Terrain Model (DEM), or a 3D model like a triangulated mesh. A discussion on experimental evaluation of the resolution of a TLS instrument is in Pesci et al. (2011). Long range TLS instruments are powerful in geomorphological surveying aimed at change detection (see e.g. Fey and Wichmann 2017).

SfM facilitates fast and inexpensive generation of accurate photorealistic point clouds and digital models by means of sequences of images taken from a ground or an aerial platform (generally an Unmanned Aerial System, UAS), or a combination of them. Good results in terms of precision and resolution require data taken in favorable and consistent light conditions without significant disturbances (like vegetation). For this reason, this technique is often used in geological and geomorphological surveying (Brunier et al. 2016; Smith et al. 2016), also including harsh environment (Rauhala et al. 2017). Tests on SfM precision and resolution show that deformation patterns of at least 3-4 cm are detectable at 250 m distance, under the condition that the unstable area is surrounded by stable areas. The resolution limit is about ~2.5 times the ground sampling distance (GSD) (Pesci et al. 2020). This paper aims at evaluating the ground deformations induced by a blast test in both natural and treated soils, from TLS and SfM surveys. Since in the test area there where staff personnel engaged in several activities and various kinds of equipment, instruments and objects, the survey scheduling was strongly constrained. Remote sensing activities were carried out within relatively short time windows (Amoroso et al. 2020a).

Test site

The full-scale blast test took place on 4 June 2018 in the Bondeno area (Ferrara, Italy) in order to study the effects of soil liquefaction and their possible mitigation by means of the installation of Rammed Aggregate Piers (RAPs). Details about the RAP improvement technique are available in Saftner et al. (2018). The geological setting of the area is characterized by liquefiable silty sands that accumulated during the late Pleistocene and Holocene, that lies on the buried external portions of the Apennine chain, where seismically active fault-fold structures exist (Toscani et al. 2009; Minarelli et al. 2016), as shown in Figure 1. Besides the local stratigraphy, where the groundwater table depths in February 2018 (GWT1) and April 2018 (GWT2) are also drawn, Figure 1 shows the results of Cone Penetration Testing (CPT) carried out before and after RAP, the soils map and the map of depth to groundwater table in Emilia-Romagna. More information can be found in Amoroso et al. (2020a). The 6.1 M_w 2012 Emilia-Romagna earthquake, which involved a portion of this region and caused the main damages in Ferrara and Modena provinces (Pondrelli et al. 2012), led to liquefaction and sand boils geographically distributed along fluvial sand deposits (Tonni et al. 2015; Amoroso et al. 2020b).

The experimental area (Figure 2) was an almost rectangular portion of a plowed field, with sides of about 40 m and 80 m respectively. For the sake of brevity, the area is called the Region of

Interest (ROI). The field was not completely flat because several clods of soil give an irregular and jagged morphology. Two zones of the ROI, named the Natural Panel (NP) and Improved Panel (IP) respectively, were armed with an array of underground sequentially detonatable charges, in eight blast holes spaced around the perimeter of a circle (10 m diameter). The charges installation and detonation induced liquefaction in the silty sand from 3.5 to 9.5 m below the ground surface. The RAP columns were drilled from the surface up to 9.5 m depth in the IP area (Figure 2). On the contrary, the NP was left in its natural state. The distance between IP and NP was about 20 m, supposed to be long enough to exclude (or to significantly reduce) a possible interaction between blast effects and to support the hypothesis of same geotechnical soil properties and characteristics. Since a quality test revealed that a few RAPs in the upper-left part of IP had a reduced effectiveness due to their construction procedures (see further details in Amoroso et al., 2020a), some main effects are expected in that localized area of IP.

For convenience, the terms B0, B1 and B2 indicate the three stages of the experiment; B0 is the condition before blasts, while B1 and B2 represent conditions after the first (in the NP area) and the second blast (in the IP area), respectively. Subsequently, B1b refers to the stage immediately preceding the second blast, i.e. a stage in which temporary effects could still be present due to a not yet completed phenomenon exhaustion. Other technical details about the experiment can be found in Amoroso et al. (2020a), where each stage of the blasting is carefully described. As mentioned above, the acquisition of accurate information about surface variations (meaning primarily liquefaction-induced subsidence) was carried out by means of two independent remote sensing techniques: TLS and UAS-based SfM, as in Pesci et al. (2018). Table 1 summarizes the test scheduling. It should be noted that, given the limited time available, only a UAS survey was carried out at B1b stage.

Ten Ground Control Points (GCPs), evenly distributed on the ROI with positions provided by GNSS (Global Navigation Satellite System) measurements, were installed for georeferencing scopes. Each GCP consisted of a target composed of two wooden arms 40 cm long forming a cross shape, fixed to the ground. Finally, 62 survey stakes driven about 30 cm into the ground along a line passing throughout the IP and NP centers allowed levelling measurements during the experiment stages, leading to time series of the relative heights variations of the upper subsoil layer. The error on stakes height measurement is ~1 mm, while the horizontal coordinates from rapid-static GNSS observations are characterized by ~1 cm error.

Remote sensing surveys and conventional ground settlement surveys

The procedure for data analysis consisted of some steps: creation of point clouds; generation of the corresponding Digital Terrain Models (DTMs), i.e. 2.5D models, from the point clouds; comparison between DTMs; mapping and interpretation of terrain variations. DTMs comparisons provided well-defined patterns of surface subsidence and terrain changes. In addition, conventional levelling surveys taken before and after blasts provided very accurate time series of punctual height variations along a reference line passing through NP and IP. These measurements were also useful for constructive criticism about remote sensing results.

TLS surveys

TLS is a very efficient technique in surveying aimed at evaluating soil subsidence because of the high spatial resolution, good accuracy and very low scans registration error, on condition that suitable viewpoints are chosen (see e.g. Benito-Calvo et al. 2018). A Teledyne Polaris instrument (Teledyne 2021), equipped with an electronic level to provide correct verticality, was mounted on a pole at about 6 m above the ground, using a Level Lift Roof device (Scan&Go 2021) and acquired, for each session, three scans, one for each of three viewpoints along a side of the ROI 40 m long (Table 1 and Figure 3). The acquisition time for each scan was about 5 minutes, leading to a dense point cloud with 5 mm sampling step at 100 m reference distance. The point clouds alignment by means of the surface matching algorithm implemented in PolyWorks software package (Innovmetric 2021), led to three multitemporal point clouds. Subsequently, the data registration into the WGS84 UTM32 reference was carried out by means of GCP coordinates.

Figure 3 shows the complete point cloud acquired before the experiment and the point clouds specifically related to the ROI, i.e. the previously mentioned rectangular study area, for each experiment stage (B0, B1 and B2) subsequently used for data analysis.

Figure 4 shows the comparison between multitemporal TLS models. In particular, the differences B1-B0, B2-B0 and B2-B1 are presented in different forms by changing the scale to gradually describe the results from both the qualitative and quantitative point of view. The rows in Figure 4 describe the results using different scales to better point out both the variations and their planimetric distribution. Since the aim is to highlight the boundaries of the deformed zones and their spatial distribution as effect of blast-induced subsidence, only the areas with negative variations are shown. In the first row there are the maps of differences Δ in the range from 0 to -2 mm. In the other rows, the maximum settlement is progressively increased by ranges of 2 cm.

Some results can be directly inferred from Figure 4: 1) the subsided area of the NP is almost circular, showing main negative values (settlement) up to about 10 cm; 2) less marked lowering reveals the presence of ejected material; 3) the IP settlement pattern is not likewise regular and shows smaller maximum values (less than 6 cm) mainly distributed in a very localized top-left part of the area because of the reduced RAP effectiveness of some piers. This fact is also independently confirmed by geoelectric surveys performed soon after the blast, that identified more significant resistivity reduction in the upper-left piers in comparison to the surrounding IP soil (Amoroso et al. 2020a); 4) regarding the B2-B1 differences, a small settlement of ~2.5 cm in the area around the NP is evidenced around the circle; 5) there is noise in B1-B0 and B2-B1 maps consisting in a range of lines, which seem to radiate from a point in the NW part of the ROI, due to a strong wind event that occurred during the second TLS survey (i.e. B1) and caused vibrations of the pole on which the scanner was installed.

A morphological map is here defined as the difference between a point cloud and a reference horizontal plane whose elevation is the mean elevation of that point cloud. Figure 5 shows the complete information, i.e. the map of differences (B2-B0) and the morphological maps (B0 and B2) with the same reference plane. The cumulative surface settlement map (B2-B0) allows the recognition and quantification of a clear subsidence “bowl” in the area around the explosive charges, with a lowering of about 6-8 cm widely distributed in the NP zone. After the second blast, a few small zones in the IP area show maximum settlements ranging from 4 to 5 cm. In particular, no more than 25% of the IP surface area shows significant changes, i.e. changes exceeding 4 cm, confirming the effectiveness of the RAP-based liquefaction mitigation.

The procedure for volume computation requires some steps. At first, only point clouds parts belonging to the deformed areas are used and modelled. For each model, a relative volume is computed with respect to a reference horizontal plane. Subsequently, the pair-by-pair volume differences lead to the results. Table 2 summarizes these results, including the settlement surface areas, i.e. 375 m^2 and 420 m^2 for NP and IP, respectively. The apparently anomalous fact that the reference area is slightly smaller (difference ~10%) in the case of NP panel is due to the presence of equipment partially obstructing this zone and that must be removed from the point cloud before the calculations. As expected, a noticeably smaller volume change characterizes the IP area.

The estimation of volume uncertainties come from an independent computation in areas not affected by deformation providing an error-coefficient for unit area. The method runs by computing volumes and volume differences with respect to a reference frame in a large portion of the ROI not affected by blasts. In this case, the volume difference is 1.57 m^3 in an area of about 980 m^2, leading to 0.0016 m^3 for unit area and, therefore, the uncertainties shown in Table 2.

A further computation of volume changes, carried out with the same approach, refers to two smaller circular areas around blast centers having 7.5 m radius and provides -3.4 ± 0.3 m^3 in NP and -1.6 ± 0.3 m^3 in IP. They represent, respectively, about 30% and 20% of the whole volume changes previously computed. These values confirm that variations in IP are no more than 50% the one in NP. However, a correction is necessary for the presence of extruded materials in NP (typically mud cones) causing an underestimation of volume loss by subsidence. Inspecting point clouds and isolating/removing materials deposited on the surface, highlight a volume underestimation of 0.9 ± 0.3 m^3. Therefore, the correct volume variation in NP is -4.3 m^3 instead of -3.4 m^3. The results show that, in terms of volume changes, the effects detected in IP were no more than about 37% of those in NP, corresponding to a 63% mitigation factor.

SfM surveys

SfM surveys were carried out by means of an UAS equipped with a DJI FC6310 camera and flying at about 20 m above the ground. The main technical specifications for the camera, including the GSD at 20 m flight height, are summarized in Table 3.

The drone flew four times in the time span from 10:00 to 16:00 (Table 1): the first time before blast (B0); the second one after the first blast (B1); the third one about two hours after B1 (B1b); the last one after the second blast (B2). For each flight, about 60 images were taken and processed by means of the PhotoScan software package, now upgraded in Metashape (Agisoft 2021), leading to the point clouds shown in Figure 6. It is interesting to note that SfM allows the recognition of the effects of groundwater leakage (bluish areas in Figure 6). A completely free approach to bundle adjustment was used, i.e. no GCPs were used to carry out the photogrammetric modeling. The image alignment was based on full-size images, without subsampling, by choosing the option 'High accuracy' in PhotoScan.

The 'High' option for dense cloud generation was selected in the last step of SfM processing, resulting in point clouds having 5 mm sampling step. Figure 7 provides details about the blast areas, pointing out local changes, mainly attributable to mud volcanoes, emissions of water, sand and silt. Note that the availability of a model related to an inter-blast time, i.e. B1b, allows the detection of variations observed after a few hours in comparison to rapid soil settlement shortly after the liquefaction and pore pressure dissipation.

The maps of differences were created following the same approach used for the TLS data analysis. The comparison between Figures 6 (SfM) and 4, 5 (TLS) shows that the same magnitudes and similar patterns of subsidence were obtained. The difference maps from SfM show greater subsidence in the NP area with respect to the IP where RAP installation reduced settlement both in space distribution and maximum subsidence. The quite similar maps from B1b-B1 and B2-B1 seem to ensure that there are no significant interactions between blasts, suggesting that 20 m distance was an appropriate choice, even if this assertion comes from surficial measures only. Finally, the TLS and SfM point clouds were registered into the same relative reference frame by means of surface matching algorithms applied to the part of the ROI far from the blasting areas. In particular, the use of targets for the registration into an external reference frame was unnecessary in this stage.

Levelling and cross-sections

Ground surface settlements for the first (B1) and the second (B2) blasts, based on the elevation change of the survey stakes, are plotted in Figure 8 along the line through the NP and IP centers. The automatic level used to for measurements was located about 20 m from the blast center, preventing liquefaction-induced settlement. Levelling measures were taken after 30-60 minutes from blasts, when excess pore pressure had probably almost fully dissipated. Reconsolidation following the blast-induced liquefaction produced a nearly symmetrical settlement pattern across the NP as shown in Figure 8 for the first blast. Maximum settlement at the center of the blast ring was ~9.5 cm and settlement decreased to zero at a distance of ~12 m from this center. Settlements within the blast ring were between 7.0 and 9.5 cm after the first blast.

The second blast produced both settlement within the IP area and some minor additional settlement in the NP one, possibly due to strain softening during the first blast sequence. The IP surface settlement due to the second blast was significantly lower than the one occurred in NP area as effect of the first blast. However, the settlement profile around the IP was not symmetric, as observed in the NP for B1, but was higher on the north side where the RAPs were characterized by lower quality, as already discussed. This result is consistent with observations from the TLS and SfM surveys.

A Sondex profilometer pipe placed at the NP and IP centers provided the measurements of settlement as a function of depth. The results show that liquefaction-induced variations primarily occurred between 3.5 and 11.0 m below the ground surface. Moreover, there is agreement between the measured surface and subsoil settlements.

Crossline inspection

The availability of 62 survey stakes placed on the line connecting the blast centers allowed a comparison between remote sensing and classical levelling data. As mentioned in section devoted to the study site description, the horizontal coordinates of the stakes were obtained by means of GNSS observations. WGS84 UTM32 reference frame was used. Moreover, the relative height of the head of each stake was measured three times (before the test, after the first blast and after the second blast).

To provide a direct comparison between TLS/SfM data and levelling data, the georeferenced TLS point clouds are used. However, for a better representation and description, the data are given in an arbitrary reference frame where the *x*-axis is the line joining the blast area centers, the *z*-axis is vertical and the *y*-axis is defined accordingly (Figure 9). Actually, two cross-sections, named A and

B respectively, were extracted from each one of the TLS point clouds on two parallel lines 0.5 m on opposite sides of the stake line. This was necessary because of the presence of stakes noising and obstructing the surface. Moreover, the used remote sensing techniques do not allow the repeated measurement of the same specific point but leads to the acquisition of point clouds distributed on the observed areas.

Figure 9 illustrates the lines of the cross-sections drawn on the ROI and the cross-sections, extracted with 5 cm sampling test, related to all the point clouds. Figure 10 shows the cross-sections related to NP and IP areas. Finally, Figure 11 shows the height differences computed along the A and B cross-sections for the three stages, which constitute the significant information about the blast-induced changes.

TLS and levelling measure different objects. The first one provides points distributed on the surface, the second one measures the head of stakes at a certain height above surface and stakes are connected to the subsoil at about 30 cm depth. Therefore, a direct comparison between TLS and levelling data is not possible. For this reason, TLS and levelling comparison refers to heights variations, even if the changes due to material accumulation on the ground cannot be measured by levelling.

Figure 12 shows TLS and levelling data over-imposed. The points extracted from DTMs (the cumulative surface variation, i.e. B2-B0, as indicated in previous figures) along the cross-section A and B profiles are shown together with the points provided by the level survey (STi). The agreement is quite good despite the presence of some interesting differences. A simple statistics allows the quantification of discrepancies between the two data sets. Figure 12 also shows a histogram with the frequency of differences between TLS and STi data. The difference with the highest frequency is -2 mm with a standard deviation (SD) of 8 mm. However, there is also a secondary peak with a mean value of -21 mm with 6 mm SD. Both the distributions appear to have almost Gaussian shape. Note that data for statistics from TLS cross-sections were interpolated at the same sampling step of levelling to use compatible data set distribution.

Some differences are clearly due to the presence of ejected material but the offset between TLS and levelling is also present in the near around of IP and NP areas. The farther from the centre the less discrepancy. These fact should be taken into account for the result interpretation: (1) the stakes are inserted into the ground, therefore they are connected to a deeper layer, more compacted than the superficial plowed terrain; (2) the extruded material cannot be observed by measuring the top of stakes but accumulate at the ground surface; (3) the levelling and TLS lines does not coincide spatially despite are very close (as above described, the cross-sections where taken at 0.5 m from the levelling line); (4) some errors in points positioning the STi into TLS reference frame could be possible due to the alignment of different frames.

Discussion

The main objectives of this study are: (1) to evaluate the quality and significance of the remote sensing measurements aimed at studying the settlement of the soil surface due to earthquake-induced or blast-induced liquefaction, and (2) to quantitatively assess the reduction in settlement allowed by the RAP-related mitigation of the liquefaction hazard.

The maps of differences provided by TLS and SfM at the various stages of the experiment provided the same qualitative and quantitative results. In particular, the deformations patterns visible in the NP and IP areas, which correspond to a natural and a treated site respectively, are significantly different. It is important to underline that remote sensing techniques allow a characterization of the soil surface over the entire study area, highlighting localized phenomena that may not be captured by other observation methods such as levelling. Moreover, TLS and SfM allow very fast surveys. Therefore, these techniques are sufficient to characterize the deformation patterns, leading to very dense point clouds suitable for both qualitative and quantitative evaluations. Note that the photogrammetric modeling was implemented with free-net bundle adjustment, i.e. the GCPs were used for the sole purpose of georeferencing the point cloud and provide, at the same time, the correct scale factor. On the other hand, although PhotoScan (or Metashape) allows the use of GCPs to constrain the bundle adjustment, not all photogrammetric software packages allow this. If a planar surface is observed from a large number of viewpoints well distributed in space, which is the case of the surface surveyed in this test, the constraint by GCPs is unnecessary.

The comparison between TLS and levelling data highlighted peculiarities related to the fact that remote sensing techniques only provide data about the soil surface. This comparison, characterized by a very high precision in height measurement (~1 mm), showed a not negligible discrepancy. This suggests that measured surficial deformation could underestimate the real settlements up to ~15%, probably due to a weak connection between surface and underlying layers. Note that the experimental field is an agricultural context and the ground is periodically moved and plowed and treated resulting in a set of loose soil elements.

These discrepancies suggest that in some specific environment the results from remote sensing require a little bit criticism for interpretation, especially in the case of data relating to agricultural areas. Although this evidence is limited to this case study only, it is to consider that data provided by Synthetic Aperture Radar (SAR) from satellite or other terrestrial, airborne or satellite remote sensing techniques are used to provide the ground deformation at regional scale, in particular the effects of liquefaction, due to a seismic event (see e.g. Chini et al. 2015). This should be taken into account both in the generation of a 3D displacement field from a 2D one (see e.g. Fernandez et al. 2018) and in the study of a numerical model that aims to reconstruct motions in depth at the fault level starting from the 2D displacement field on the ground surface (Currenti et al. 2010).

Regarding the geotechnical aspects of the described blast test, the settlement occurred in the NP resulted in a bowl-shaped settlement pattern over a wide area leading to subsidence of up to 10 cm. This settlement was accompanied by the ejection of water and sands from subsoil. In contrast, in the IP area the effects were quite reduced, involving a smaller portion of the area and only subjected to a few centimeters of subsidence. In particular, no more than 25% of the IP area was affected by settlement greater than 6 cm and this appears to be an area where the RAP installation was poorly performed. Moreover, almost no ejection of sand or water occurred in such an area. This reduction in ejecta produced by the RAP group is significant considering that ejecta is estimated to have been responsible for more than 33% of the damage in the Christchurch New Zealand earthquake sequence (Quigley et al. 2013).

Finally, the precision of TLS and SfM data was adequate for a complete characterization of the ground settlement variations for both NP and IP areas. The results also showed that TLS and SfM can provide reliable volume calculations, including an estimation of the volume of the ejected material. In particular, the results highlighted that the subsidence in areas improved by RAP was meanly reduced by a factor 50%. In the area where the RAP-based improvement was greater, the volume change did not exceed 37% of that in the non-improved area.

Conclusions

Performance and limits of TLS and SfM for the characterization of the ground surface deformation of silty sand areas affected by earthquake-induced liquefaction were studied in controlled conditions thanks to a blast test. In particular, an untreated natural (NP) area and an area treated with a group of RAPs for improved liquefaction resistance (IP) were studied before the test, after a first blast in the NP area and after a second blast in the IP area.

The maps of settlement difference provided by TLS and SfM were qualitatively and quantitatively coherent. These remote sensing techniques showed that the settlement in the NP area was widely distributed over a large area, with maximum subsidence of ~10 cm, whereas in the IP a smaller area was affected by of 5 to 6 cm subsidence. Besides some interesting advantages of TLS and SfM, including the rapidity of data acquisition and processing, also a problem must be taken into account. The deformation obtained from these remote sensing techniques could sometimes underestimate the real subsidence effects up to about 15%, as the comparison with the levelling survey pointed out. These evidences from this specific study case cannot be exported as a general result but indicate that a carefully criticism is needed in data interpretation instead. They will be useful in planning the next blast test scheduled for 2021 in a new test site in Emilia-Romagna. The results showed that, despite this systematism, remote sensing techniques allowed reliable volume calculations and, in particular, highlighted the RAP performance.

Data Availability Statement

Some or all data, models, or code that support the findings of this study are available from the corresponding author upon reasonable request. The available data are: all images, all point clouds, all PhotoScan and PolyWorks projects.

Acknowledgements

The study was primarily funded by Geopier® Foundation Company (Davidson NC, USA). Financial contributions to this research activity were also provided by INGV-FIRB Abruzzo project ("Indagini ad alta risoluzione per la stima della pericolosità e del rischio sismico nelle aree colpite dal terremoto del 6 aprile 2009", http://progettoabruzzo.rm.ingv.it/it) and by INGV-Abruzzo Region project ("Indagini di geologia,sismologia e geodesia per la mitigazione del rischio sismico", L.R. n. 37/2016). Special thanks to: Releo s.r.l. (Ferrara, Italy), who provided the installation of the Rammed Aggregate Piers free of charge; Brigham Young University, who contributed to the realization of the blast test experiment in terms of personnel and technical equipment; to the blaster

Andrea Carpena for the services and for the aerial images; Teledyne (Dario Conforti), Scan&Go srl (Massimo Secchia) and iMages SpA (Donato Marcantonio) for their invaluable help in laser scanning monitoring; Fawzi Doumaz (INGV) for flight organization and UAV images; Michele Perboni, who kindly guested the experimental activities, Bondeno Municipality (in particular Stefano Ansaloni, Olga Mantovani and Elena Bonora) and Emilia-Romagna Region (Luca Martelli), who provided all the necessary support to realize the research in collaboration with the other local authorities (Ferrara Prefecture, Ferrara Province, Local Civil Protection, Police).

References

Agisoft, 2021. “PhotoScan/Metashape web site.” Accessed April 20, 2021. http://www.agisoft.com.

Amoroso, S., K.M. Rollins, P. Andersen, G. Gottardi, L. Tonni, M.F. García Martínez, K. Wissmann, L. Minarelli, C. Comina, D. Fontana, D., et al., 2020a. “Blast-induced liquefaction in silty sands for full-scale testing of ground improvement methods: Insights from a multidisciplinary study.” *Engineering Geology* 265: 105437. https://doi.org/10.1016/j.enggeo.2019.105437.

Amoroso, S., C. Comina, and D. Marchetti, 2020b. “Combined P- and S-wave measurements by seismic dilatometer test (SPDMT): a case history in Bondeno (Emilia Romagna, Italy).” *Geotechnical Testing Journal* 43: 2. https://doi.org/10.1520/GTJ20180233.

Amoroso, S., G. Milana, K. M. Rollins, C. Comina, L. Minarelli, M. R. Manuel, P. Monaco, et al. 2017. “The First Italian Blast-Induced Liquefaction Test (Mirabello, Emilia-Romagna, Italy): Description of the Experiment and Preliminary Results.” *Annals of Geophysics* 60 (5): S0556. https://doi.org/10.4401/ag-7415.

Ashford, S.A., K.M. Rollins, and J.D. Lane, 2004. “Blast-Induced Liquefaction for Full-Scale Foundation Testing.” *Journal of Geotechnical & Geoenvironmental Engineering* 130 (8), 798-806. https://doi.org/10.1061/(ASCE)1090-0241(2004)130:8(798).

Benito-Calvo, A., F. Gutiérrez, A. Martínez-Fernández, D. Carbonel, T. Karampaglidis, G. Desir, J. Sevil, J. Guerrero, I. Fabregat, and Á. García-Arnay, 2018. "4D Monitoring of Active Sinkholes with a Terrestrial Laser Scanner (TLS): A Case Study in the Evaporite Karst of the Ebro Valley, NE Spain." *Remote Sensing* 10(4): 571. https://doi.org/10.3390/rs10040571.

Brunier, G., J. Fleury, J.E. Anthony, V. Pothin, C. Vella, P. Dussouillez, A. Gardel, and E. Michaud, 2016. "Structure-from-Motion photogrammetry for high-resolution coastal and fluvial geomorphic surveys." *Géomorphologie* 22 (2), 147–161. https://doi.org/10.4000/geomorphologie.11358.

Chini, M., M. Albano, M. Saroli, L. Pulvirenti, M. Moro, C. Bignami, E. Falcucci, S. Gori, G. Modoni, N. Pierdicca, and S. Stramondo, 2015. "Coseismic liquefaction phenomenon analysis by COSMO-SkyMed: 2012 Emilia (Italy) earthquake." *International Journal of Applied Earth Observation and Geoinformation* 39, 65-78. https://doi.org/10.1016/j.jag.2015.02.008.

Currenti, G., A. Bonaccorso, C. Del Negro, F. Guglielmino, D. Scandura, and E. Boschi, 2010. "FEM-based inversion for heterogeneous fault mechanisms: application at Etna volcano by DInSAR data." *Geophysical Journal International* 183, 765-733. https://doi.org/10.1111/j.1365-246X.2010.04769.x

EN, 2004. *Eurocode 8: Design of Structures for Earthquake Resistance – Part 5: Foundations, Retaining Structures and Geotechnical Aspects*. Bruxelles: CEN European Committee for Standardization.

Fey, C., and V. Wichmann, 2017. "Long- range terrestrial laser scanning for geomorphological change detection in alpine terrain – handling uncertainties." *Earth Surface Processes and Landforms* 42, 789-802. https://doi.org/10.1002/esp.4022.

Fernandez, J., J.F. Prieto, J. Escayo, A.G. Camacho, F. Luzón, K.F. Tiampo, M. Palano, T. Abajo, E. Pérez, J. Velasco, J., et al. 2018. "Modeling the two- and three-dimensional displacement field in

Lorca, Spain, subsidence and the global implications.” *Scientific Reports* 8: 14782. https://doi.org/10.1038/s41598-018-33128-0

Finno, R.J., A.P. Gallant, and P.J. Sabatini, 2016. “Evaluating Ground Improvement after Blast Densification at the Oakridge Landfill.” *Journal of Geotechnical & Geoenvironmental Engineering* 142 (1), 1-13. https://doi.org/10.1061/(ASCE)GT.1943-5606.0001365.

Giona Bucci, M., P. Villamor, P. Almond, M. Tuttle, M. Stringer, W. Ries, C. Smith, M. Hodge, and M. Watson, 2018. “Associations between sediment architecture and liquefaction susceptibility in fluvial settings: The 2010–2011 Canterbury Earthquake Sequence, New Zealand.” *Engineering Geology* 237, 181-197. https://doi.org/10.1016/j.enggeo.2018.01.013.

Gutiérrez, F., M. Zarroca, R. Linares, C. Roqué, D. Carbonel, J. Guerrero, J.P. McCalpin, X. Comas, and A.H. Cooper, 2018. “Identifying the boundaries of sinkholes and subsidence areas via trenching and establishing setback distances.” *Engineering Geology* 233, 255-268. https://doi.org/10.1016/j.enggeo.2017.12.015.

Győri, E., L. Tóth, Z. Gráczer, and T. Katona, 2011. “Liquefaction and Post-Liquefaction Settlement Assessment – A Probabilistic Approach.” *Acta Geodaetica et Geophysica Hungarica* 46 (3), 347-369. https://doi.org/10.1556/AGeod.46.2011.3.6.

Hu, J. and H. Liu, 2019. “Identification of ground motion intensity measure and its application for predicting soil liquefaction potential based on the Bayesian network method.” *Engineering Geology* 248, 34-49. https://doi.org/10.1016/j.enggeo.2018.11.006.

Innovmetric 2021. “PolyWorks web site.” Accessed: April 20, 2021. https://www.innovmetric.com.

Minarelli, L., S. Amoroso, G. Tarabusi, M. Stefani, and G. Pulelli, 2016. “Down-hole geophysical characterization of middle-upper Quaternary sequences in the Apennine Foredeep, Mirabello, Italy.” *Annals of Geophysics* 59 (5): S0543. https://doi.org/10.4401/ag-7114.

Pesci, A., G. Teza, V. Kastelic, and M.M.C. Carafa, 2020. “Resolution and precision of fast, long range terrestrial photogrammetric surveying aimed at detecting slope changes.” *Journal of*

Surveying Engineering 146 (4): 04020017-1-13. https://doi.org/10.1061/(asce)su.1943-5428.0000328.

Pesci, A., S. Amoroso, G. Teza, and L. Minarelli, 2018. "Characterisation of soil deformation due to blast-induced liquefaction by UAV-based photogrammetry and terrestrial laser scanning." *International Journal of Remote Sensing* 39 (22), 8317-8336. https://doi.org/10.1080/01431161.2018.1484960.

Pesci, A., G. Teza, and E. Bonali, 2011. "Terrestrial laser scanner resolution: numerical simulations and experiments on spatial sampling optimization." *Remote Sensing* 3 (1), 167-184. https://doi.org/10.3390/rs3010167.

Pondrelli, S., S. Salimbeni, P. Perfetti, and P. Danecek, 2012. "Quick regional centroid moment tensor solutions for the Emilia 2012 (northern Italy) seismic sequence." *Annals of Geophysics* 55 (4), 615-621. https://doi.org/10.4401/ag-6146.

Quigley, M.C., S. Bastin, and B.A. Bradley, 2013. "Recurrent liquefaction in Christchurch, New Zealand, during the Canterbury earthquake sequence." *Geology*, 41 (4), 419-422. https://doi.org/10.1130/G33944.1.

Rauhala, A., A. Tuomela, C. Davids, and P.M. Rossi, 2017. "UAV Remote Sensing Surveillance of a Mine Tailings Impoundment in Sub-Arctic Conditions." *Remote Sensing* 9: 1318. https://doi.org/10.3390/rs9121318.

Saftner, D.A., R.A. Green, and R.D. Hryciw, 2015. "Use of explosives to investigate liquefaction resistance of aged sand deposits." *Engineering Geology* 199, 140-147. https://doi.org/10.1016/j.enggeo.2015.11.002.

Scan&Go, 2021. "Level lift roof web site." Accessed April 20, 2021. https://www.scan-go.eu/product/level-lift-roof-evo/

Saftner, D.A., J. Zheng, R.A. Green, R. Hryciw, and K. Wissmann, 2018. “Rammed aggregate pier installation effect on soil properties.” *Institution of Civil Engineers-Ground Improvement* 171 (2), 63-73. https://doi.org/10.1680/jgrim.16.00021

Smith, M.W., J.L. Carrivick, and D.J. Quincey, 2016. Structure from motion photogrammetry in physical geography. *Progress in Physical Geography* 40 (2), 247-275. https://doi.org/ 10.1177/0309133315615805.

Teledyne, 2021. “Teledyne Polaris laser scanning website.” Accessed April 20, 2021. https://www.teledyneoptech.com/en/products/static-3d-survey/polaris/

Tonni, L., G. Gottardi, S. Amoroso, R. Bardotti, I. Bonzi, A. Chiaradonna, A. d’Onofrio, V. Fioravante, A. Ghinelli, D. Giretti, et al., 2015. “Interpreting the deformation phenomena triggered by the 2012 Emilia seismic sequence on the Canale Diversivo di Burana banks.” *Italian Geotechical Journal* 49 (2), 28-38. http://www.associazionegeotecnica.it/sites/default/files/rig/2_2015_028ton.pdf.

Toscani, G., P. Burrato, D. Di Bucci, S. Seno, and G. Valensise, 2009. “Plio-Quaternary tectonic evolution of the northern Apennines thrust fronts (Bologna-Ferrara section, Italy): seismotectonic implications.” *Italian Journal of Geosciences* 128, 605-613. https://doi.org/10.3301/IJG.2009.128.2.605

Vosselman, G., and H.G. Maas, eds. 2010. *Airborne and terrestrial laser scanning*. Boca Raton FL: CRC Press.

Wentz, F.J., S. van Ballegooy, K.M. Rollins, S.A. Ashford, and M.J. Olsen, 2015. “Large Scale Testing of Shallow Ground Improvements Using Blast-Induced Liquefaction.” Paper presented at the 6th International Conference on Earthquake Geotechnical Engineering (6ICEGE), Christchurch, NZ, November 1-4. Accessed April 20, 2021. https://secure.tcc.co.nz/ei/images/ICEGE15%20Papers/Wentz_530.00.pdf.

Table 1. Test scheduling. Times refer to Central European Time (CET), i.e. Coordinate Universal Time + 1h.

Event	Pre-blast	First blast [a]	Inter-blast		Second blast [b]	Post-blast
TSL survey [c]	11:00 (B0)	---	12:50 (B1)	---	---	16:00 (B2)
UAV flight [c]	10:10 (B0)	---	12:40 (B1)	15:05 (B1b)	---	15:50 (B2)
Blast [d]	---	12:15	---	---	15:30	

[a] blast in NP area
[d] blast in IP area
[c] Times at mean survey
[d] Actual times

Table 2. Volume variations due to blasts in NP and IP areas.

Case	ΔV (m^3)	
	NP [a]	IP [b]
B2-B0	-12.5 ± 0.7	-6.3 ± 0.6
B1-B0	-11.3 ± 0.7	0.8 ± 0.6
B2-B1	-1.3 ± 1.0	-7.1 ± 0.8

[a] Reference area: 375 m^2
[b] Reference area: 420 m^2

Table 3. Main camera technical specifications and image parameters.

Feature/parameter	Unit	DIJ FC6310
Focal length	mm	8.8
Aperture (f-stop)	-	f/5.6
Equivalent focal length 35 mm	mm	24
Crop factor	-	2.7
Sensor number of pixels	-	5472 × 3648
Sensor size	mm × mm	13.2 × 8.8
Pixel side	mm	0.00241
Exposition time	S	1/400
GSD at 20 m flight	mm	5.5

Figure 1

Click here to access/download;Figure;Fig1.tif

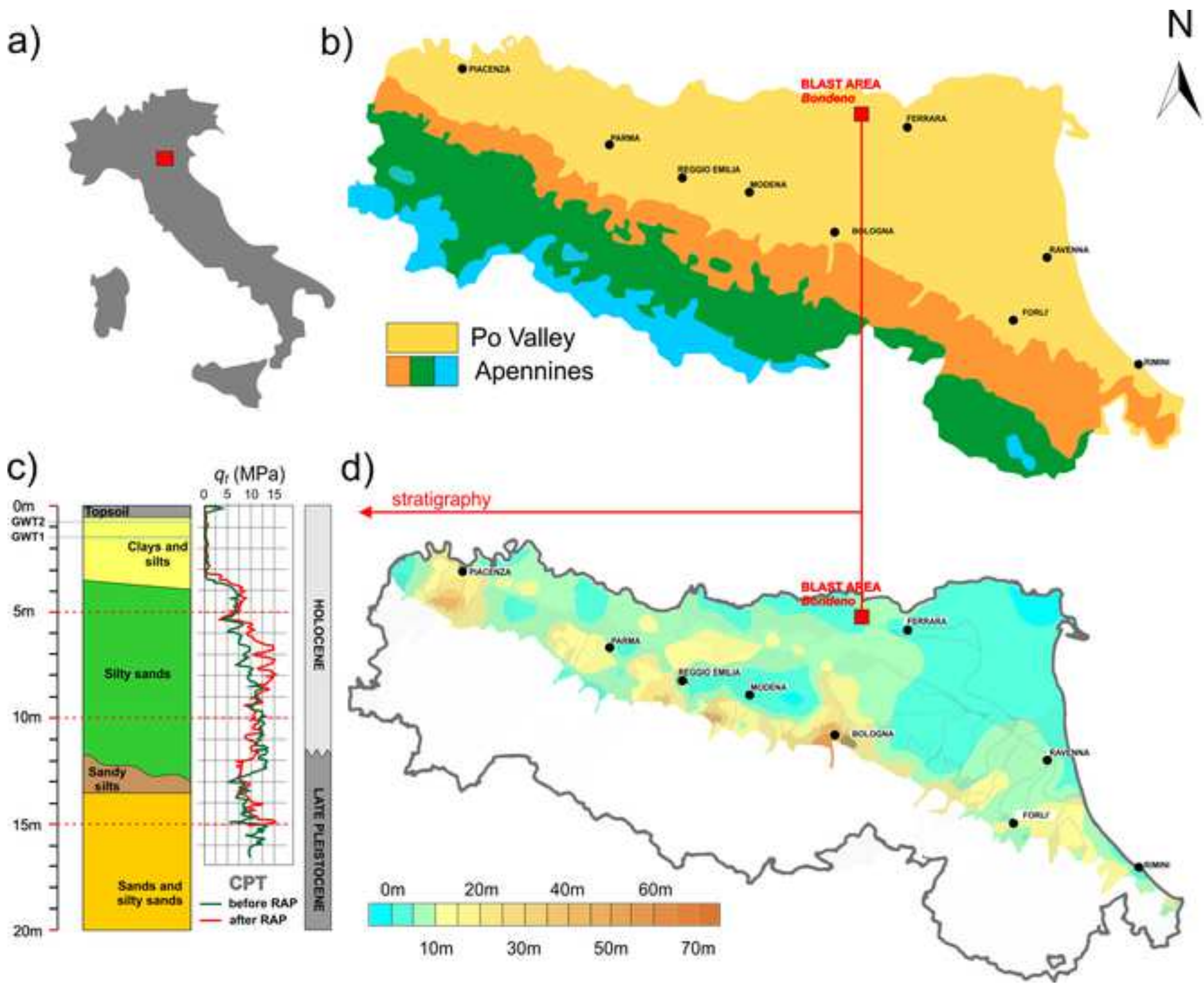

Figure 2

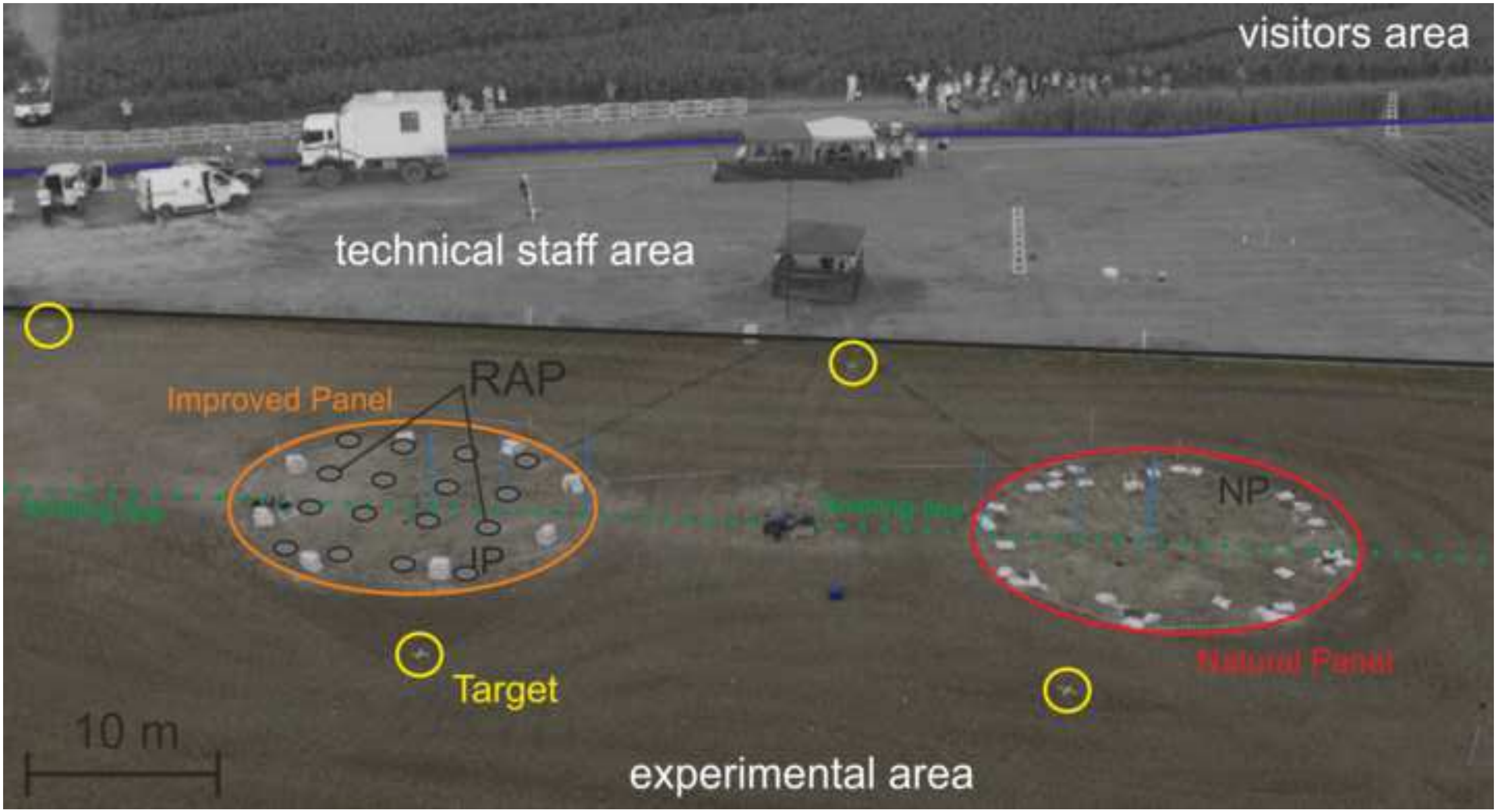
visitors area
technical staff area
RAP
Improved Panel
NP
IP
Target
10 m
experimental area

Figure 3

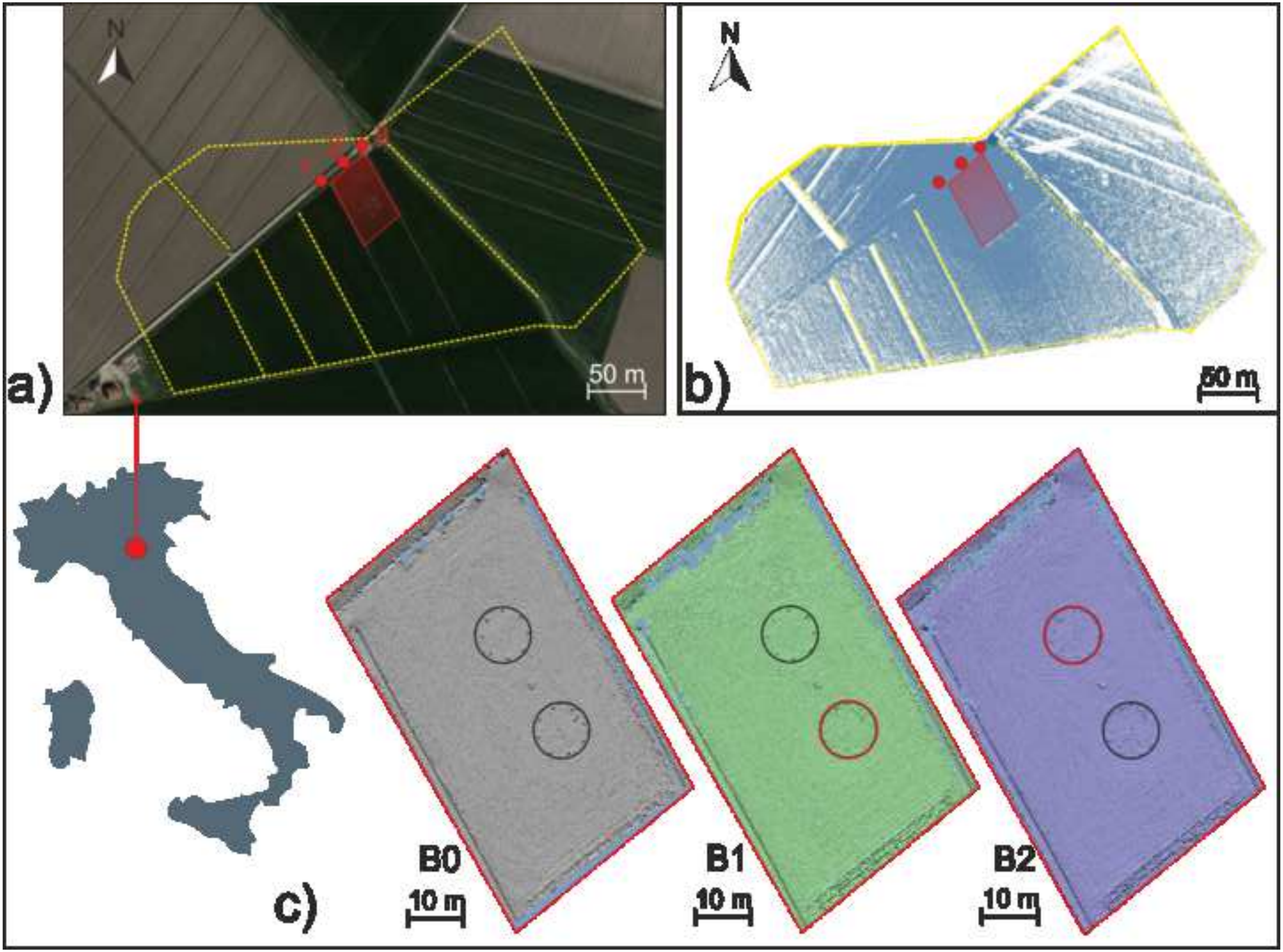

Figure 4

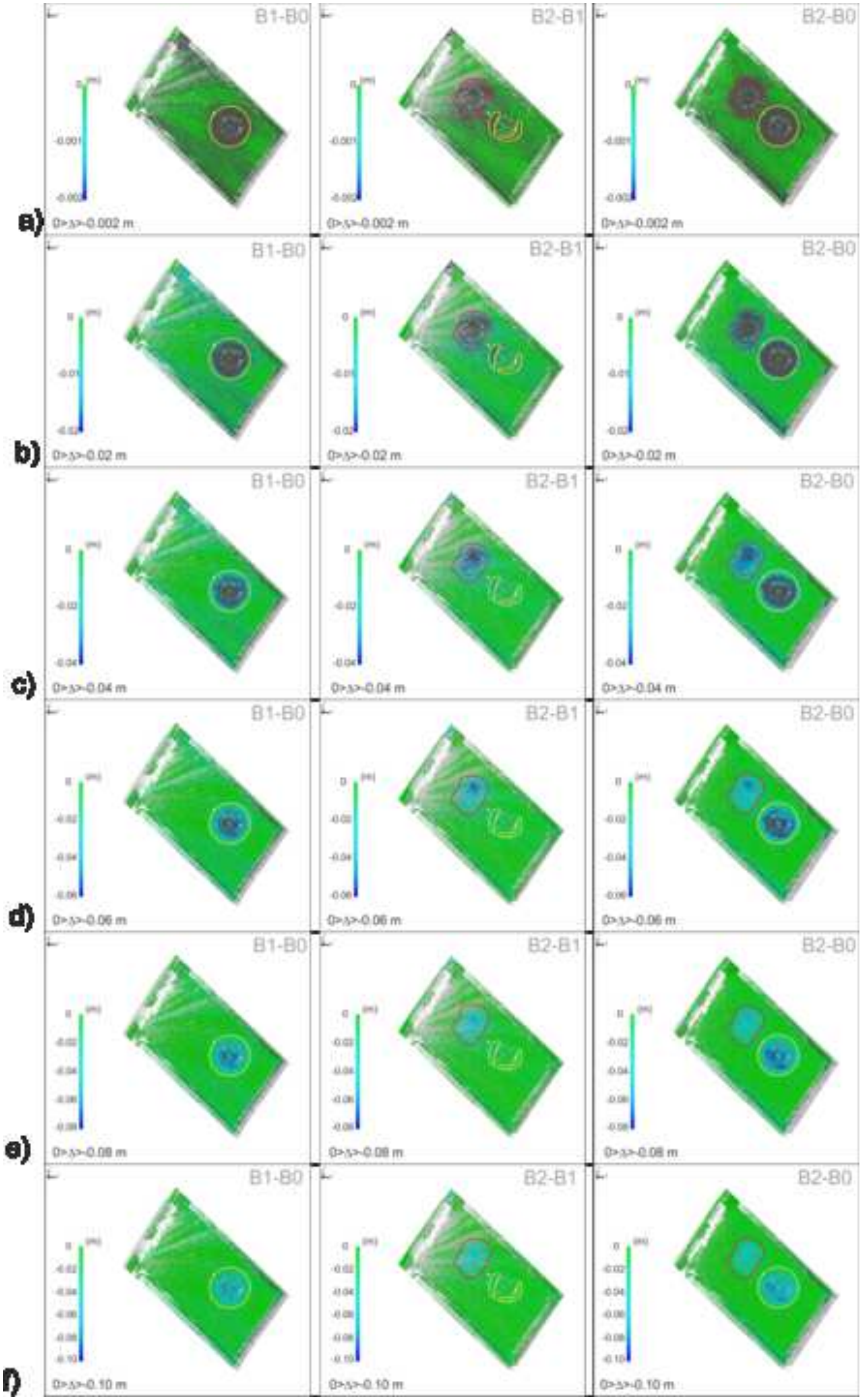
B1-B0
B2-B1
B2-B0
a)
0>Δ>-0.002 m
b)
0>Δ>-0.02 m
c)
0>Δ>-0.04 m
d)
0>Δ>-0.06 m
e)
0>Δ>-0.08 m
f)
0>Δ>-0.10 m

Figure 5

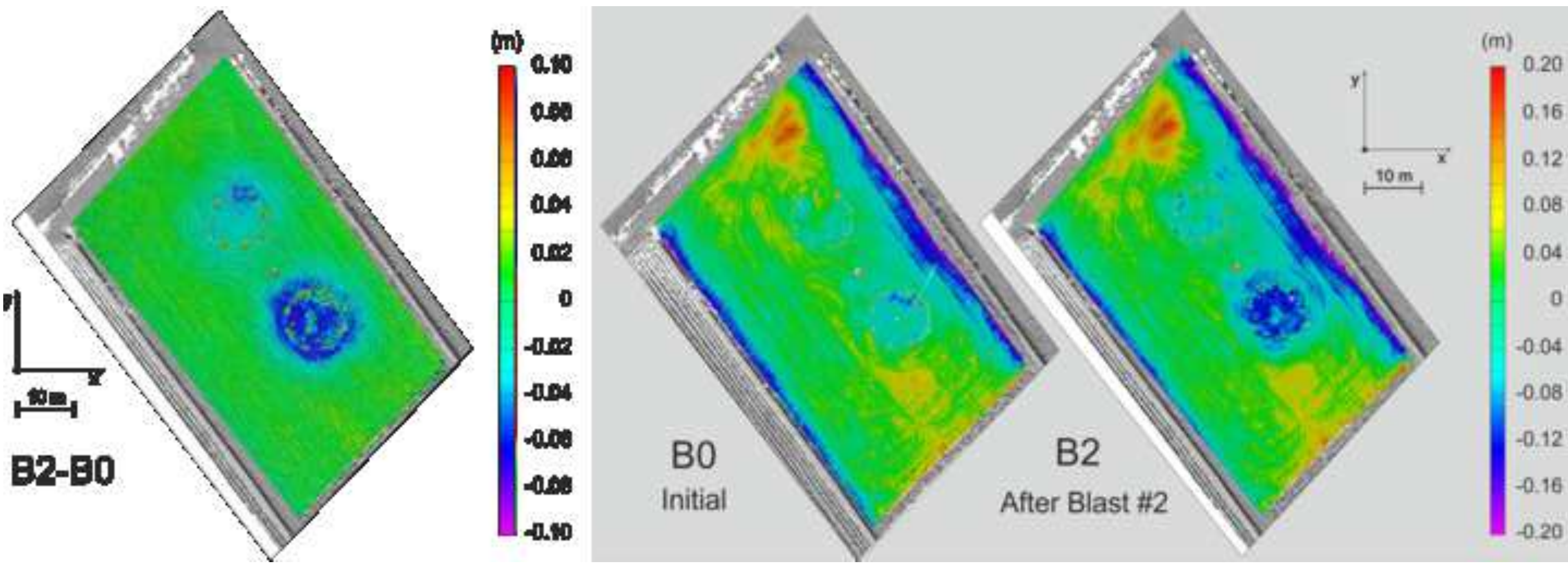

B2-B0
10 m
(m)
0.10
0.08
0.06
0.04
0.02
0
-0.02
-0.04
-0.06
-0.08
-0.10
B0
Initial
B2
After Blast #2
y
x
10 m
(m)
0.20
0.16
0.12
0.08
0.04
0
-0.04
-0.08
-0.12
-0.16
-0.20

Figure 6

Click here to access/download;Figure;FIG6 NEW.tif

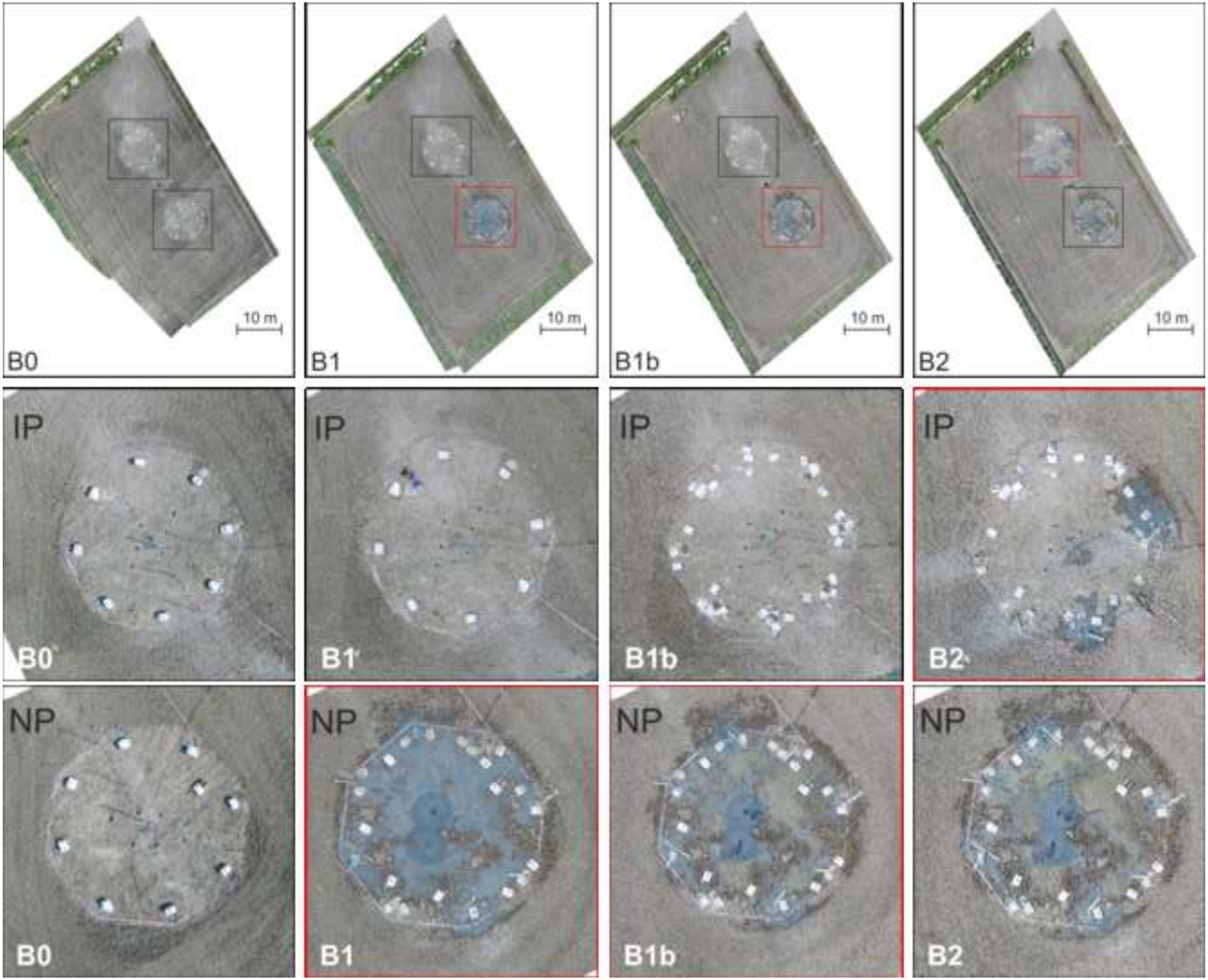

Figure 7

Click here to access/download;Figure;FIG7_scala giusta NEW.tif

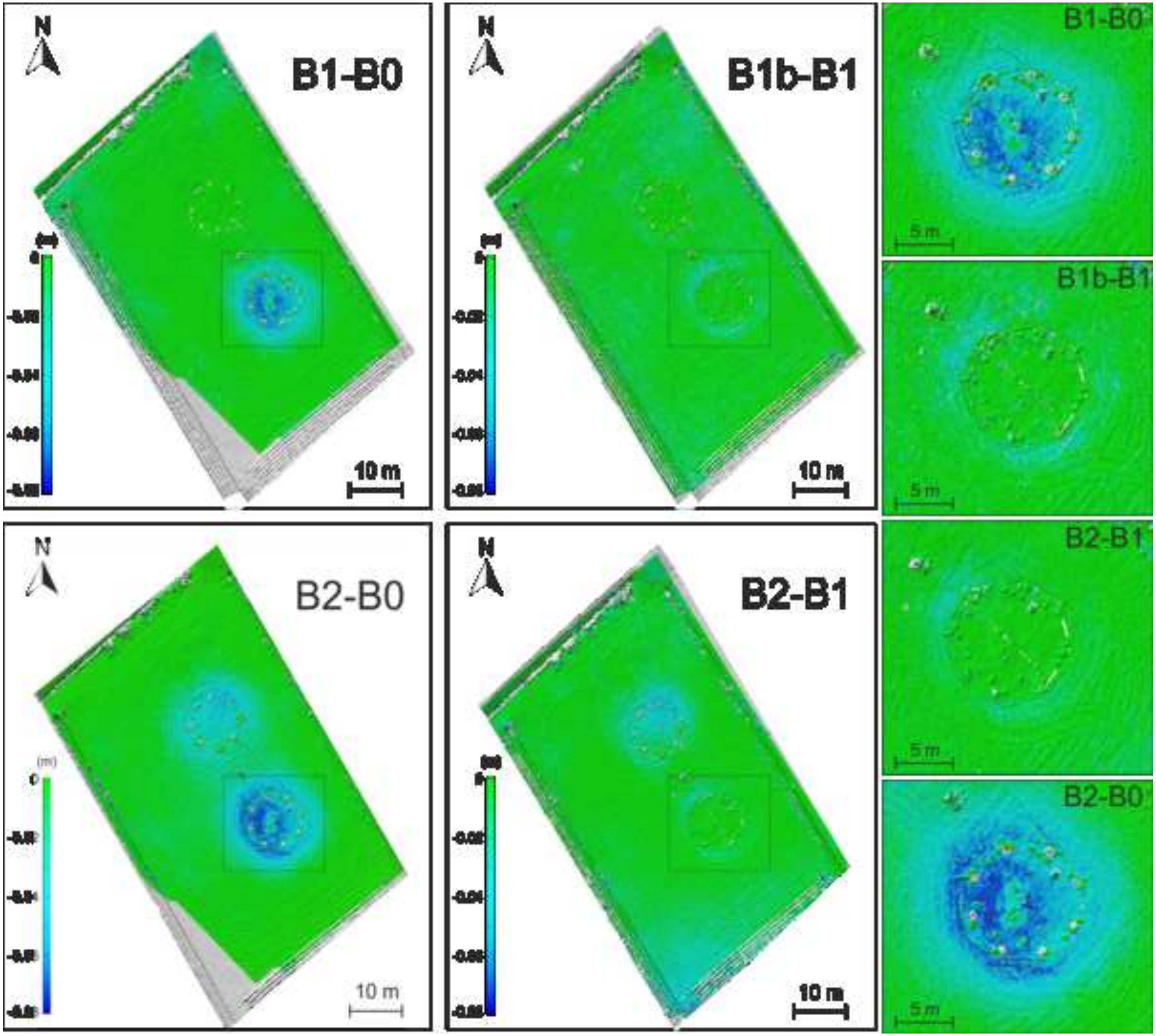

Figure 8

Click here to access/download;Figure;Fig8.tif

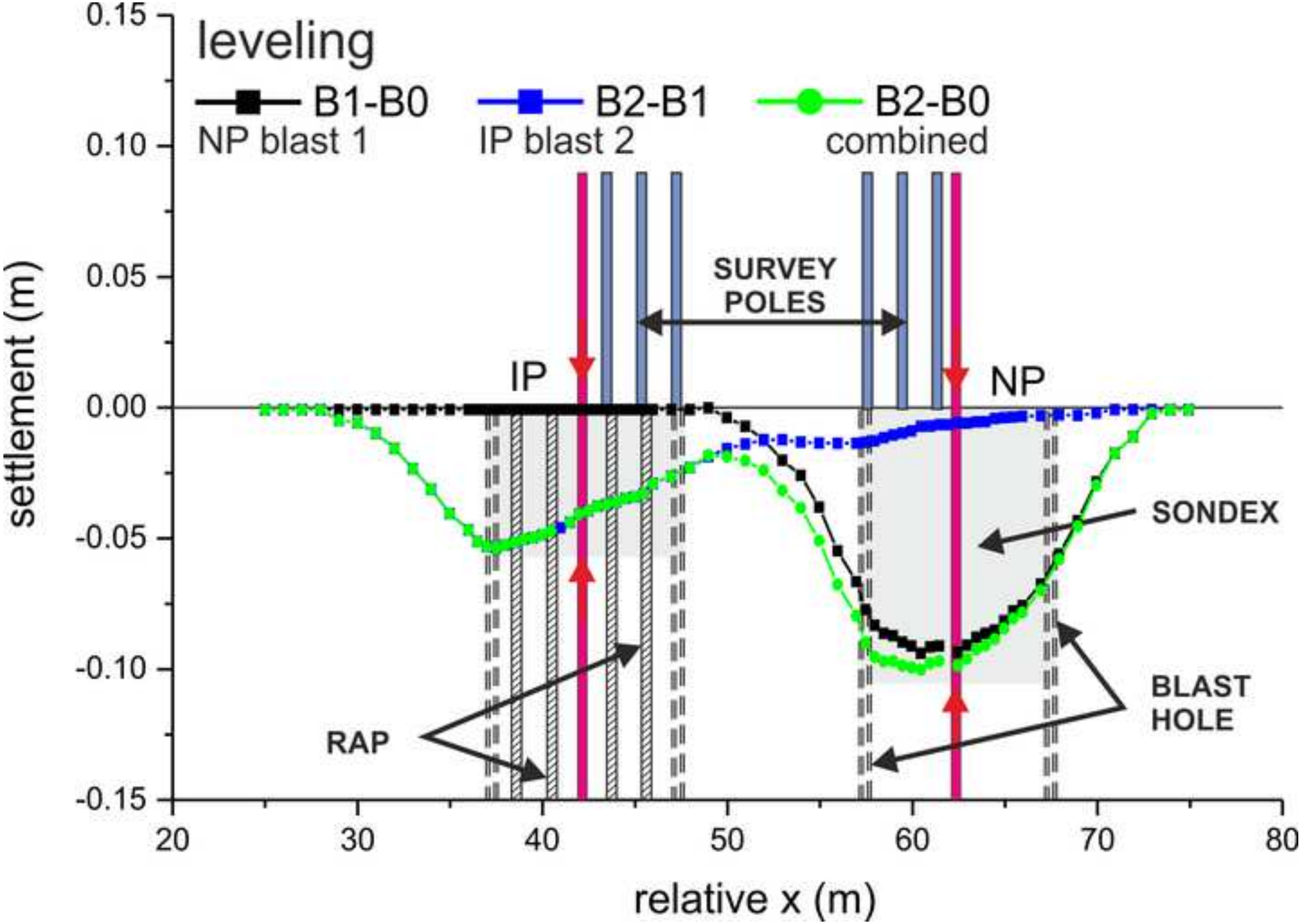

Figure 9

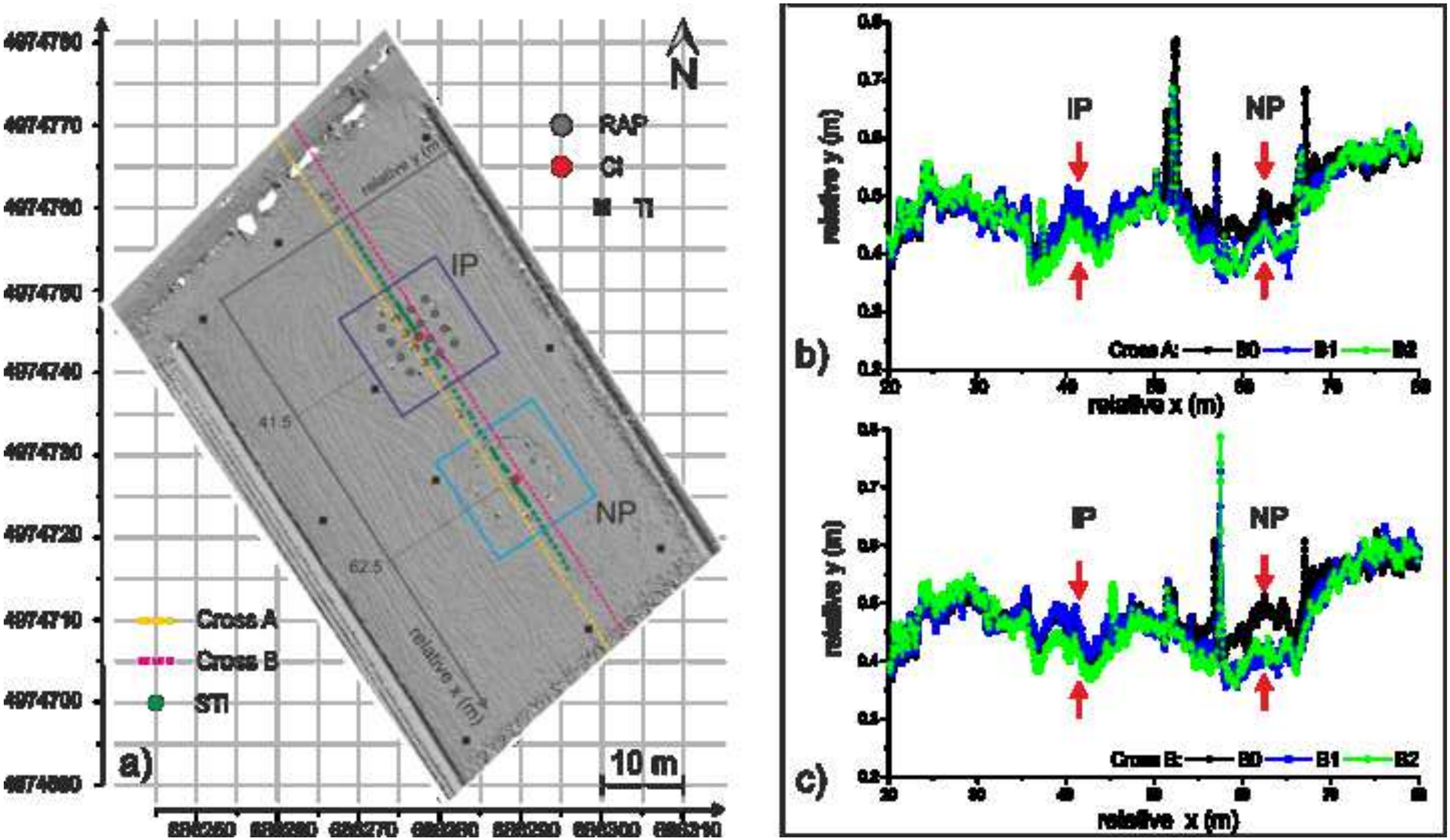
N
RAP
CI
TI
IP
NP
relative y (m)
relative x (m)
41.5
62.5
Cross A
Cross B
STI
a)
10 m
b)
c)
Cross A: B0 B1 B2
Cross B: B0 B1 B2
relative y (m)
relative x (m)

Figure 10

Click here to access/download;Figure;FIG10 NEW.tif

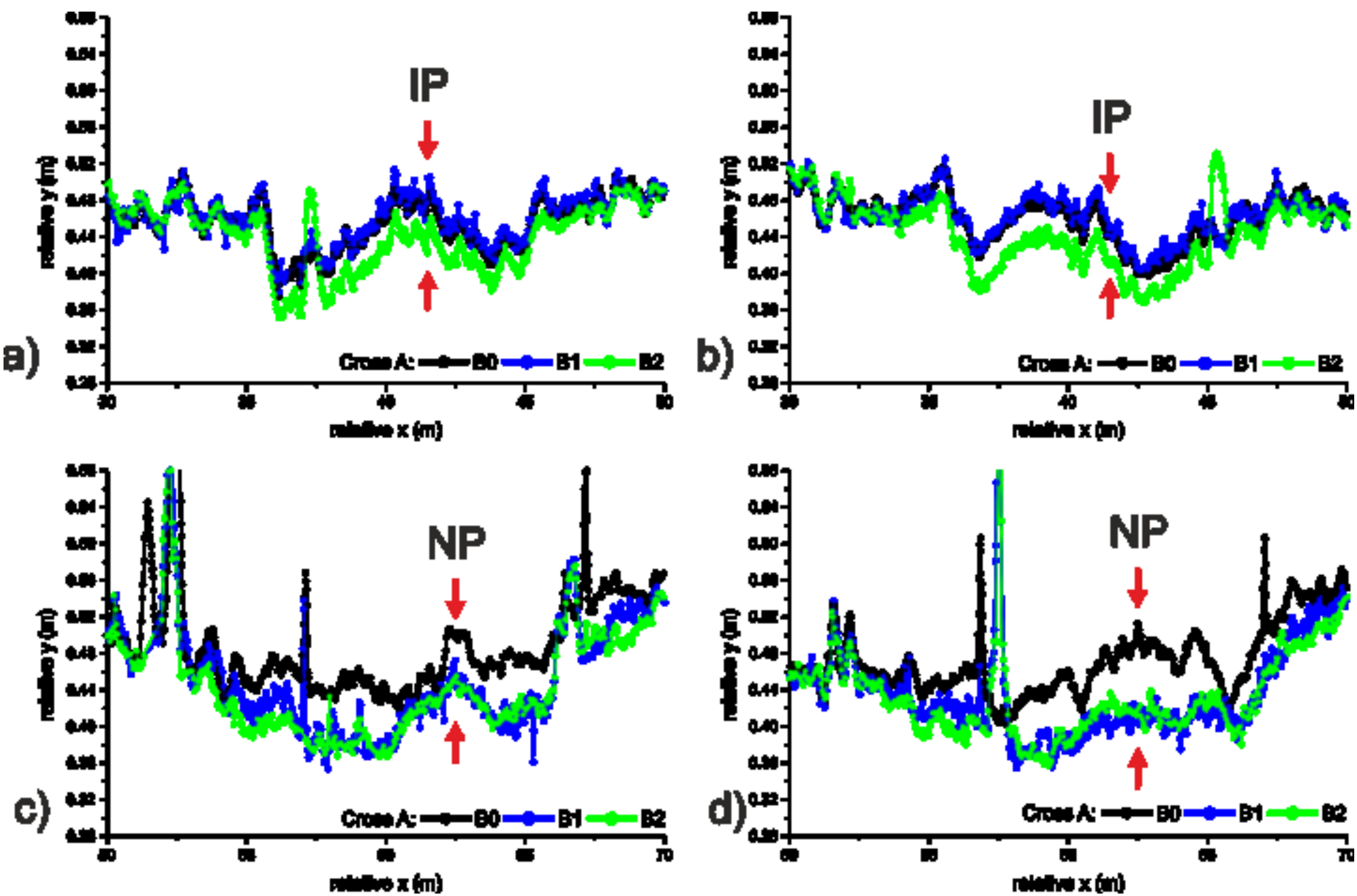

Figure 11

Click here to access/download;Figure;FIG11 NEW.tif

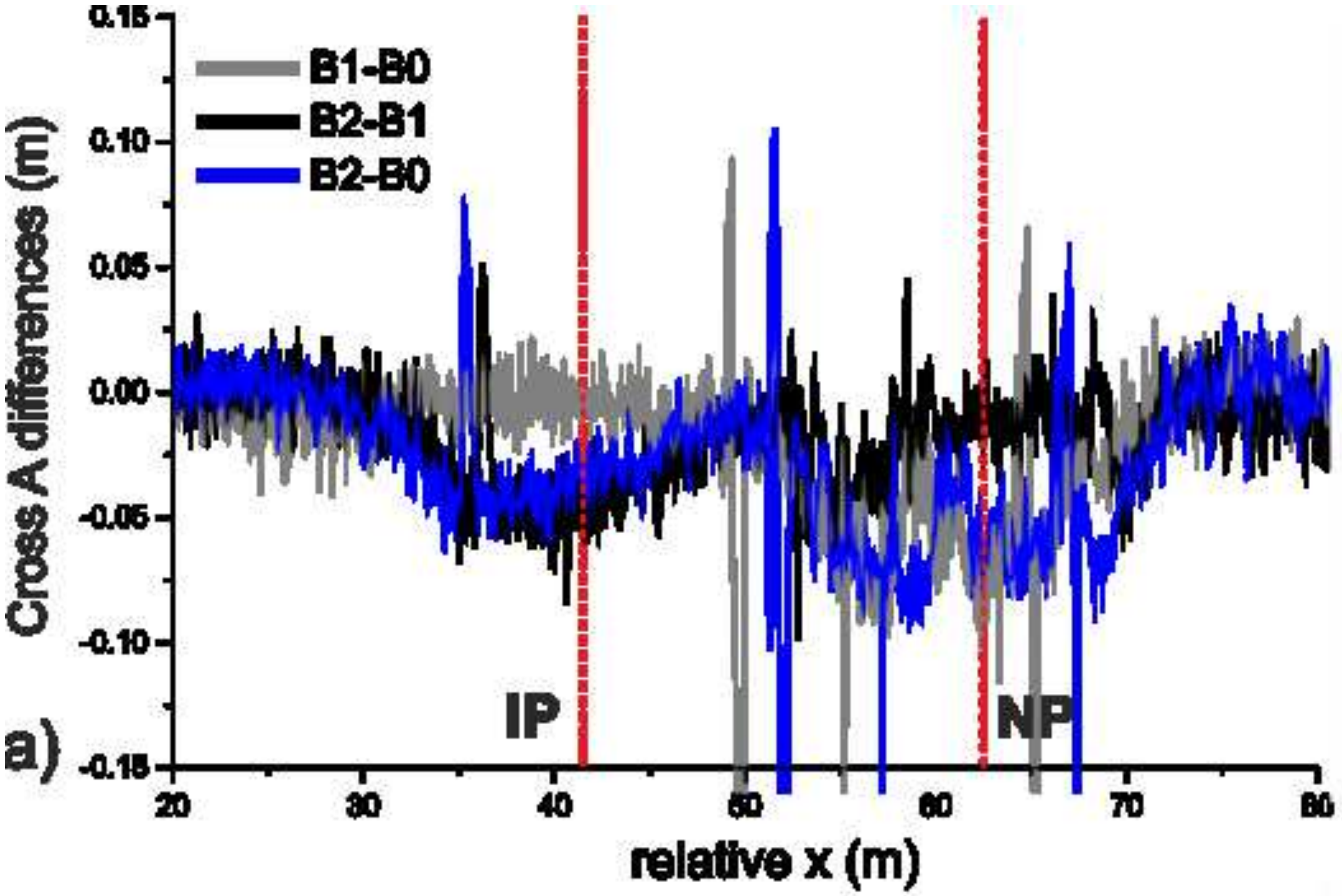

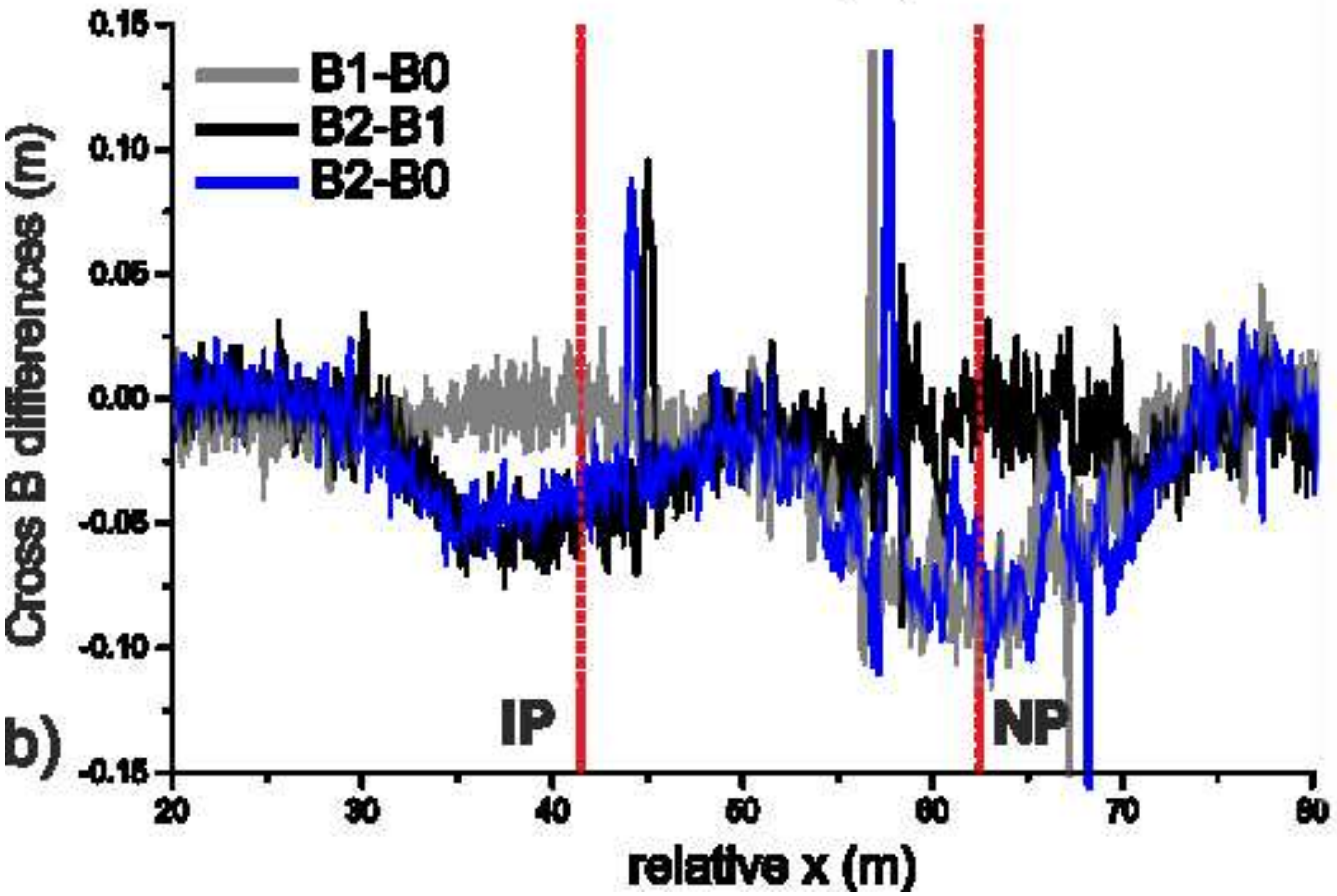

Figure 12

Click here to access/download;Figure;FIG12_diff e stat NEW.tif

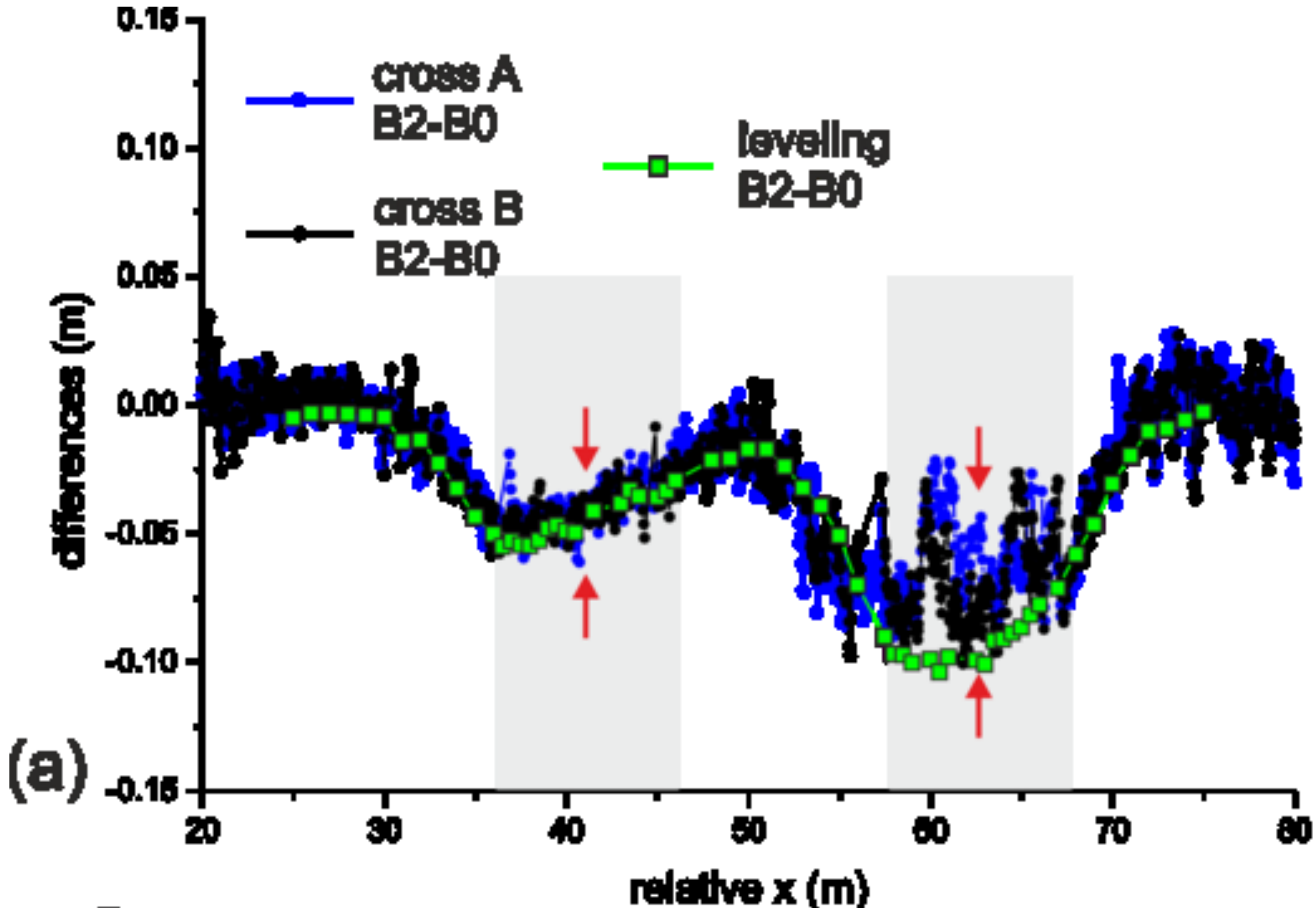

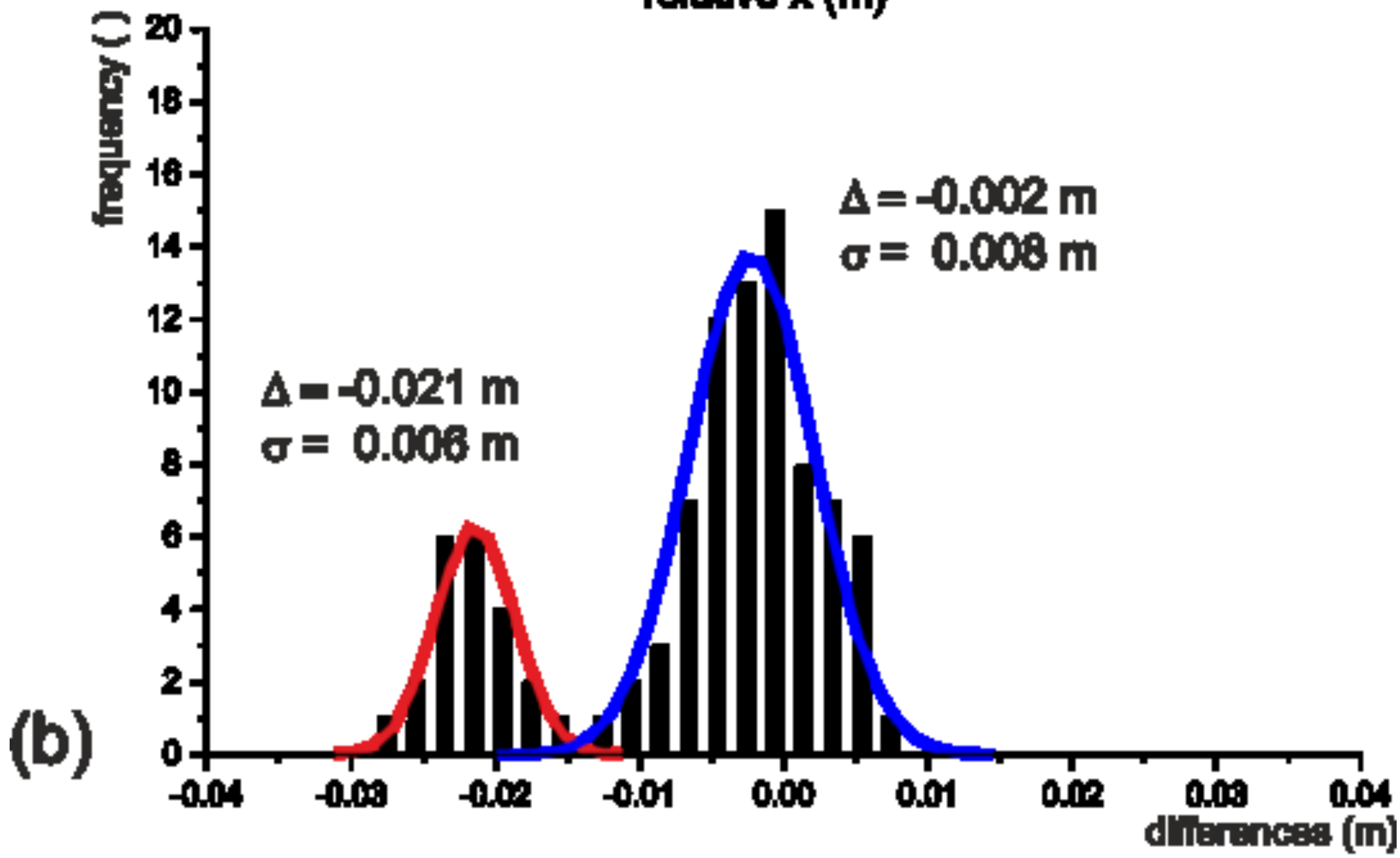

Figure captions

Figure 1. Basic geological/geotechnical information about Bondeno area: a) localization; b) schematic soils map of Emilia-Romagna, where plain and Apennine Mountains of different elevations are shows; c) soil stratigraphy, where the groundwater table depths in February 2018 (GWT1) and April 2018 (GWT2) are also shown, and CPT results in terms of total cone resistance (q_t) before and after RAP; d) map of depth to groundwater table.

Figure 2. A qualitative description of the experimental field from aerial images taken by a stationary drone before blasting. The two blast areas (IP and NP) are highlighted, together with the main topographical details such as the levelling line (dotted line) and the targets used to materialize the GCPs for georeferencing purposes.

Figure 3. TLS survey: a) aerial image of the area on which the TLS point cloud boundary (i.e. the ROI) is superimposed and where the TLS viewpoints are shown (points 1, 2 and 3); b) the complete point cloud obtained from the first survey(before the experiment); c) the three TLS point clouds of the ROI, where B0, B1 and B2 means the three experiment stages, i.e. pre-blast, post-blast1 and post-blast2.

Figure 4. Maps of differences in settlement (negative values), obtained from multitemporal TLS surveys, B1-B0, B2-B1, B2-B0 in the range: a) [-2 mm, 0]; b) [-20 mm, 0]; c) [-40 mm, 0]; d) [-60 mm, 0]; e) [-80 mm, 0]; f) [-100 mm, 0].

Figure 5. B2-B0 map of differences and B0 and B2 morphological maps representing the terrain surficial topography before and after the blast experiment.

Figure 6. SfM point clouds for B0, B1, B1b and B2 stages and zoom in NP and IP areas. The mean flight times are also shown (top right angle of each panel).

Figure 7. Comparison between the SfM models in the more suitable difference scale, i.e. the range [-8 cm, 0]. On the right column, a zoom-in of the NP area shows the “bowl” shaped settlement pattern around the blast center.

Figure 8. A comparison of ground settlement measurements obtained 30 minutes after the first blast in the NP, and the second blast in the IP along a line between the centers of the NP and IP. The combined settlement from B1 and B2 is shown with circles.

Figure 9. Cross-section generation: a) ROI, levelling points, targets and schematic features, where STi indicate the levelling stakes, Ti the targets for georeferencing, and Ci the blast area centers; b) B0, B1 and B2 from cross-section A (Cross A), where the arrows identify the centers of each blast panel; c) B0, B1 and B2 from cross-section B (Cross B).

Figure 10. Cross-sections generated from TLS data for B0, B1 and B2 stages: a) A cross-section, IP panel; b) B cross-section, IP panel; c) A cross-section, NP panel; d) B cross-section, NP panel. Arrows indicate the centers of each blast panel.

Figure 11. Height differences obtained from TLS data: a) along A cross-section; b) along B cross-section. The centers of NP and IP areas are indicated by the dashed lines.

Figure 12. a) Cumulative lowering, i.e. related to B2-B0, obtained from TLS along the cross-sections; b) histogram of differences between levelling and TLS elevations. Arrows identify the centers of each blast panel.